A New Path Planning Algorithm Using a GNSS Localization Error Map for UAVs in an Urban Area

Guohao Zhang and Li-Ta Hsu

Interdisciplinary Division of Aeronautical and Aviation Engineering, The Hong Kong Polytechnic University, Hong Kong

ABSTRACT

The mission of future parcel delivery will be performed by unmanned aerial vehicles (UAVs). However, the localization of global navigation satellite systems (GNSS) in urban areas experiences the notorious multipath effect and non-line-of-sight (NLOS) reception, which could potentially generate approximately 50 meters of positioning error. This misleading localization result can be hazardous for UAV applications in GNSS-challenged areas. Due to multipath complexity, there is no general solution to eliminate this effect. A solution to guide UAV operation is to plan an optimal route that smartly avoids the area with a strong multipath effect. To achieve this goal, the impact of the multipath effect in terms of positioning error at different locations must be predicted. This paper proposes to simulate the reflection route by a ray-tracing technique, aided by predicted satellite positions and the widely available 3D building model. Thus, the multipath effect in the pseudorange domain can be simulated using the reflection route and multipath noise envelope, according to specific correlator designs. By reconstructing the multipath-biased pseudorange domain, the predicted positioning error can be obtained using a least square positioning method. Finally, the predicted GNSS error distribution of a target area can be further constructed. A new A* path planning algorithm is developed to combine with the GNSS error distribution. This paper designs a new cost function to consider both the distance to the destination and the positioning error at each grid. By comparing the conventional and the proposed path planning algorithms, the planned paths of the proposed methods experienced fewer positioning errors, which can lead to safer routes for UAVs in urban areas.

1. Introduction

Unmanned aerial vehicles (UAV) are widely used in military and civilian applications, such as military reconnaissance, disaster search and rescue [1] and future package delivery [2]. In recent years, the development of multi-rotor UAV provides a carrier of high controllability and flexibility. These characteristics allow employing UAVs to enable many potential civilian applications. The operation of a UAV is highly dependent on its positioning sensors. The sensors provide an accurate position of the UAV to facilitate the UAV's navigation throughout the operation. The most common sensor is the global navigation satellite system (GNSS) receiver. By receiving satellite signals and calculating the distance between the satellite and receiver, the location of the UAV is able to be determined. As UAVs become more employable for civilian applications, they are required to operate in areas closer to the public, including urban areas. Urban areas are surrounded by a large number of buildings, which are obstacles for UAVs. Operating UAVs in these areas is highly restricted for the purpose of assuring safety. The precision of the localization closely influences the performance and safety of UAVs in urban areas. However, the conventional localization method of GNSS is not reliable for urban applications [3]. The accuracy of GNSS positioning is highly affected by satellite signal blockage and the multipath effect. Since more satellites from different constellations have been recently launched, the total number of satellites could become sufficient in an urban area. The major challenge for GNSS localization is still the multipath effect. It occurs when a user device receives signal reflections, resulting in the aggregate signals deceiving the receiver tracking loop to induce an additional signal delay [4]. Especially when the number of clean measurements is limited, the GNSS positioning result will be highly deteriorated by the multipath signal [5]. Currently, the multipath error has no complete solution but only remedies that mitigate such effects.

To improve the localization accuracy in urban areas, a general approach is to implement additional sensors to compensate for inaccurate GNSS solutions. A popular method is to integrate an inertial measurement unit (IMU) and GNSS to form a complementary integration system to obtain accurate and stable positioning performance [6]. Recent research also uses a light detection and ranging (LiDAR) scanner to detect the surrounding obstacles and achieve localization via simultaneous localization and mapping (SLAM) technology [7]. SLAM can also improve the performance of localization in urban areas [8]. These methods are able to obtain an accurate localization result, but extra devices add weight to the UAV. This is could be excessive for a UAV

with a limited payload. In addition, high computation loads shorten the operation time. Researchers also employ on-board stereo vision systems to conduct visual SLAM to achieve localization and obstacle avoidance in GPS-denied areas [9]. However, without the initialization by a GNSS solution, the visual SLAM can only provide the relative position information instead of an absolute position. However, GNSS is still the only sensor system that can provide the absolute positioning result. To ensure that the safety of the UAV will not be affected by the misleading localization in an urban area, this paper proposes a new path planning algorithm to avoid having it fly in the areas with an erroneous GNSS localization result.

There are different approaches of path planning to determine the optimal path [10]. One approach is to use a grid method to divide the environment into serval grids and then calculate the cost of each step and select the lowest cost. Thus, the shortest path to the destination can be found. This path planning method is well-known as the Dijkstra algorithm [11]. By further utilizing the heuristic searching process, the A* algorithm was developed and achieved higher efficiency compared to the Dijkstra algorithm [12-15]. The A* method has been applied in an urban area, avoiding the problem of quadcopters crashing into buildings by constructing constraints of obstacles [16]. Many improved path planning algorithms are developed based on the A* algorithm. Considering the physical characteristics of aircraft, the A* algorithm is improved with extra constraints such as heading [17] and turning [18], resulting in a more appropriate route for aircraft. The A* path planning method is also capable of including extra information from the environment to determine the optimal path. A cost map of the environment can be designed to evaluate different factors during the flight, such as the operating risk [19, 20] and signal strength [21, 22]. By merging the cost map into the A* cost function, an ideal path can be determined, adapting to the operating requirements for different environments. Since A* normally requires high computation, a light-assisting method is proposed to aid A* by searching fewer grids [23]. In addition, its dynamic searching speed is improved in [24, 25]. The A* algorithm is efficient for searching a global optimized path and convenient for adapting to the requirements for different environments by adjusting the cost function. The major limitation is the computer load and memory usage when addressing large environments [26]. Another popular path planning approach is to build artificial potential fields in the environment as attractive and repulsive fields for destinations and obstacles, respectively. The path will be planned by the displacement due to the overall force. This algorithm has been used to avoid obstacles with a low computational load, enabling it to be more likely to

operate in real-time [27]. Its improvements are also developed by different researchers. New potential field methods are developed to improve controllability for complex environments [28] and to cooperate with sensor detection for real-time indoor operation [29]. However, the potential field method greatly suffers from the local minimal issue [10]. The cancellation of the force results in the aircraft failing to reach the destination and becoming trapped in the middle [30]. Another path planning approach such as the genetic algorithm [31] is developed based on genetic characteristics to determine the optimal path. The genetic algorithm is a nondeterministic algorithm that is able to cope with the ill-behaved path planning problem, especially for a dynamic or gradient information-lacking environment [32]. Although it has robust performance, the genetic algorithm is time-consuming with a high computational load [33]. The genetic algorithm may even be unable to obtain the global optimal solution on time because of the premature convergence issue [34]. Performance analysis and review of the various path planning methods can be found at [35]. In this study, the path planning is based on a predicted positioning error map and does not require real-time onboard processing. The complex distribution of the positioning error level may easily cause the local minimal problem for a potential field method. Meanwhile, the positioning error prediction map is usually effective within an hour, which is suitable for a medium computation method. Based on the above comparison of different path planning approaches, the A* method is selected in this study due to its robustness and moderated computation load.

The target application of this study is parcel delivery using autonomous quadcopters. A quadcopter has the advantages of flexibility of its movement and ease of control. In general, the flight route of a quadcopter is in a fixed altitude. This fixed-height route is able to simplify the mission and movement of a quadcopter. In this paper, as shown in Fig. 1, the process of a quadcopter flying to the destination from the starting point will be planned as follows: 1) take-off and climb to a certain height; 2) fly based on a pre-planned route at the selected height; and 3) reach the destination horizontally and land vertically. The vertical movement of the UAV is usually based on a standalone barometer [36, 37]. In the other words, the GPS positioning error will only slightly influence the UAV in the operation of take-off and landing. Moreover, the UAV altitude is commonly measured by multi-sensor integrated solutions such as the barometer aided attitude and heading reference system (AHRS), which is able to achieve 2 meters of nominal height accuracy [38]. Therefore, the path planning will be processed on a 2D map with a selected height.

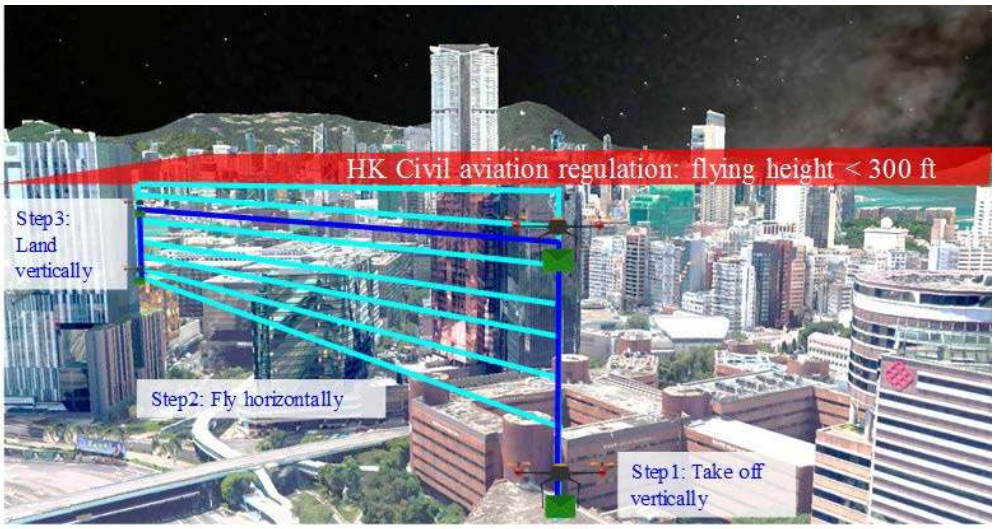

Fig. 1. Proposed flight procedure to deliver a parcel by an autonomous quadcopter.

Regarding the 2D path planning, this paper uses A* path planning cooperating with a predicted GNSS localization error map and building model to plan an optimal path in an urban area. The first result is reported in [39]. By predicting the satellites' positions through almanac data and simulating signal reflection paths by a 3D building model and ray-tracing technique, the multipath effect and non-line-of-sight (NLOS) reception can be modeled. After processing the predicted line-of-sight (LOS) and the multipath signals of a specified location, its positioning error can also be predicted. By processing all locations within the target area, the positioning error map can be generated. Because the error map is based on prediction, an offline planning method is preferred. We hence propose a new A* algorithm to take advantage of the predicted error distribution. The positioning error on each grid is used as an additional factor in the cost function. It means the higher positioning error denotes the larger traveling cost. By considering the positioning error, the UAV is able to find a path between a start point and destination that avoids both the obstacles (building in urban areas) and hazardous GPS-biased area at the same time. By comparing the result with the conventional A* algorithm and the conventional potential field method, the proposed A* path planning can plan a path that experiences less GPS error, namely, a path that is safer with a relatively short traveling distance for the UAV.

This paper is composed of 5 sections. In section 2, the generation of the predicted positioning error map is introduced. In section 3, the details of the proposed A* path planning algorithm based

on the error map are presented. In section 4, the verification of the multipath prediction model is shown. The result of the proposed path planning algorithm is evaluated. Finally, conclusions are drawn in section 5.

2. Prediction of GPS Positioning Error in an Urban Canyon

GPS positioning performance is affected by several factors, including satellite clock/orbit bias, atmospheric delays, receiver thermal noise and multipath delays [40]. The measurement errors originate from time delays due to the effect of the error sources mentioned above. The equation is given as follows:

$$\delta t_D = \delta t_{atm} + \delta t_{noise} + \delta t_{mp} + \delta t_{sat} \quad (1)$$

The overall time offset δt_D is the sum of different delays, including the atmosphere errors δt_{atm}, the receiver thermal noise δt_{noise}, multipath offset δt_{mp} and satellite clock and orbit bias δt_{sat}. There are several models to mitigate or eliminate the errors above. The atmospheric delay is caused from the signal traveling through the ionosphere and troposphere layers, where the satellite signals are influenced by free electrons and free-propagation effects. Fortunately, these errors can be eliminated by a differential GPS technique (DGPS) [41]. In general, the receiver thermal noise in the current device is less than the order of a decimeter, which is negligible compared to other errors. The multipath error is caused by receiving the reflected signals. Due to the extra traveling distance from reflection, the signal experiences a transporting time error, which further influences the correctness of the pseudorange measurement. The multipath effect is highly dependent on the surrounding environment; hence, DGPS cannot mitigate it. There are several methods to coarsely mitigate multipath effects, such as sophisticated discriminator designs and hardware enhanced antennas [42]. However, there is still no complete solution to eliminate this effect. When the UAV operation area is settled in an urban area with many high surrounding buildings, the multipath effect will be very severe, resulting in it becoming the dominant factor for GPS positioning accuracy. In this study, we focus on the positioning error introduced by the multipath effect. The first goal of this paper is to construct a predicted GPS positioning error map in a target area. To accomplish this, we were inspired by a previously developed 3D map aided by GPS positioning

methods [43]. The 3D building model used is constructed via Google Earth. We create the outline of the building to fit in the 3D model in Google Earth. For complicated building structures with different outlines along their height, the building is separated into different polygons. The simulated area selected is an urban area in Kowloon, Hong Kong, which is demonstrated in Fig. 2.

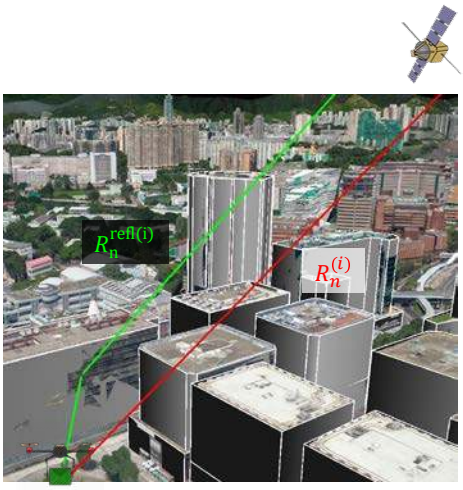

Fig. 2 Constructed 3-dimensional building model and ray-tracing simulation.

We use the building model and ray-tracing simulation to track the signal transmission path through a direct and reflection path. The position of the satellite can be predicted by the broadcast almanac. Given the satellite and receiver location, the direct signal transmission path can be easily determined. The reflection path is simulated by the ray-tracking technique. We assume that reflection follows the law of reflection. If we can find a valid reflection point on the 3D building model, then the reflection path can be simulated as shown in Fig. 2. If there are multiple reflection paths that are identified for a single satellite, then the path with the shortest transporting distance is regarded as the main multipath effect. This paper not only simulates the multipath but also NLOS effects. For the NLOS, its simulation is relatively simple. It is modeled as the reflection path $R_{\mathrm{n}}^{\mathrm{refl(i)}}$ that subtracts the direct path $R_n^{(i)}$ as below:

$$\varepsilon_n^{\mathrm{refl}(i)} = R_{\mathrm{n}}^{\mathrm{refl(i)}} - R_n^{(i)}, \varepsilon_n^{refl(i)} \in NLOS \tag{2}$$

where the superscript $^{(i)}$ denotes the index of the satellite and the subscript $_n$ denotes the index of grid points. It is interesting to note that the NLOS delay can also be modeled by the elevation angle [44]. In the other words, it is possible to model without the 3D building model. The multipath effect on the pseudorange domain is also determined by the design of the correlator in the receiver code tracking loop. Different correlator behaviors act differently in terms of the multipath noise envelope [45]. This paper selects a strobe correlator [46] to model its noise envelope *NE*, which is modeled based on correlator spacing and the relative signal strength of reflection compared to LOS. Heuristically, we assume that the multipath effect is approximately 6 dB weaker than the LOS signal, and the spacing of the strobe correlator is 0.2 chip. The multipath *NE* function based on this assumption is depicted in Fig. 3. The x-axis denotes the multipath relative delay, which is $R_{\mathrm{n}}^{\mathrm{refl(i)}} - R_n^{(i)}$, and the y-axis is the multipath delay in the pseudorange domain.

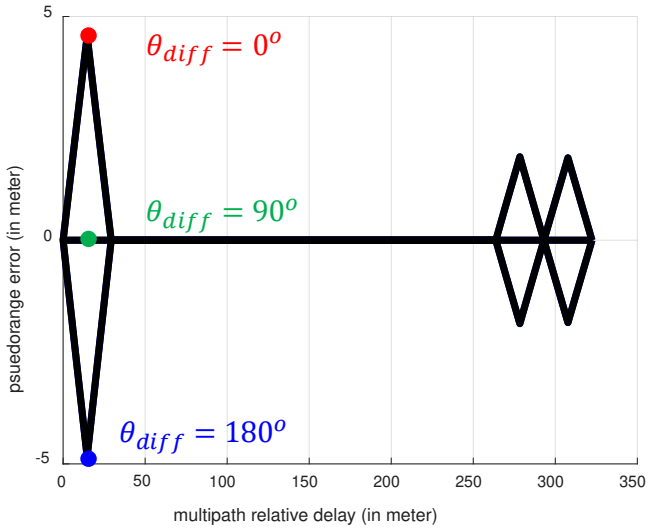

Fig. 3. Assumed noise envelope function of the strobe correlator with 0.2 chip spacing for GPS L1 C/A signal.

Thus, the multipath can be modeled as shown below.

$$\varepsilon_n^{\mathrm{refl}(i)} = NE\left(R_{\mathrm{n}}^{\mathrm{refl(i)}} - R_n^{(i)}, \theta_{diff}\right), \varepsilon_n^{refl(i)} \in Multipath \tag{3}$$

where θ_{diff} denotes the carrier phase difference between the direct and reflected signal. It is very difficult to estimate the carrier difference by ray-tracing because it requires the building model at centimeter-level accuracy [Lau Lawance]. Thus, this method only considers the carrier difference of 0^o; in other words, the upper bound of the *NE* function to cover the multipath error. Comparing (2) and (3), the NLOS is solely based on the additional traveling distance. Thus, it would induce a larger positioning error compared to the multipath. By means of the strobe correlator, the multipath with a large reflecting distance will only induce a small pseudorange error [45]. Focusing on the multipath effect on positioning error and neglecting other errors, the simulated pseudorange is given as:

$$\rho_n^{(i)} = R_n^{(i)} + \varepsilon_n^{\mathrm{refl}(i)} \tag{4}$$

where $\rho_n^{(i)}$is the predicted pseudorange, determined as the sum of the geometric distance $R_n^{(i)}$, which is determined via the ground reference location $P_n^{(i)}$, the satellite position $X_n^{(i)}$ and the multipath signal delay distance $\varepsilon_n^{\mathrm{refl}(i)}$. After simulating all the available satellites, the pseudorange can be used to calculate the predicted GPS positioning result. In this study, we assume the user device clock and the satellite clocks are perfectly synchronized, and hence, the positioning calculation is given as:

$$\Delta\rho_n^{(i)} = \hat{\rho}_n^{(i)} - \rho_n^{(i)} \tag{5}$$

$$\Delta x_n = (H_n^T H_n)^{-1} H_n^T \Delta\rho_n^{(i)} \tag{6}$$

$$x_{n,predict} = \hat{x}_n + \Delta x_n \tag{7}$$

where the approximate receiver position location is assumed as $\hat{x}^{(i)}$ with an unknown difference $\Delta x^{(i)}$ to the actual location. For the i^{th} satellite, $\hat{\rho}_n^{(i)}$ denotes the geometric distance between the approximate location and the i^{th} satellite. $\rho_n^{(i)}$ denotes the predicted pseudorange. The pseudorange difference $\Delta\rho_n^{(i)}$ can be calculated. With the direction cosine matrix of pseudorange H_n and the

pseudorange differences, the difference Δx_n can be solved via the iterative least square method. The predicted positioning solution x_n can be determined by correcting the approximate location with Δx_n. After obtaining $x_{n,predict}$ for the n^{th} grid point, the positioning error ε_n^{pe} due to the multipath effect can be calculated by comparing it with the real n^{th} location $x_{n,real}$ as follows:

$$\varepsilon_n^{pe} = \left\| x_{n,predict} - x_{n,real} \right\| \tag{8}$$

where $\|\cdot\|$ denotes norm calculation. Repeating the process for all the grids in the target area, the map of the predicted positioning error can be finally obtained as shown in Fig. 4 below. The color of the right panel of Fig. 4 denotes the 2D positioning error of each grid. It can be seen that the positioning error exceeds 20 meters in most of the places of our testing area.

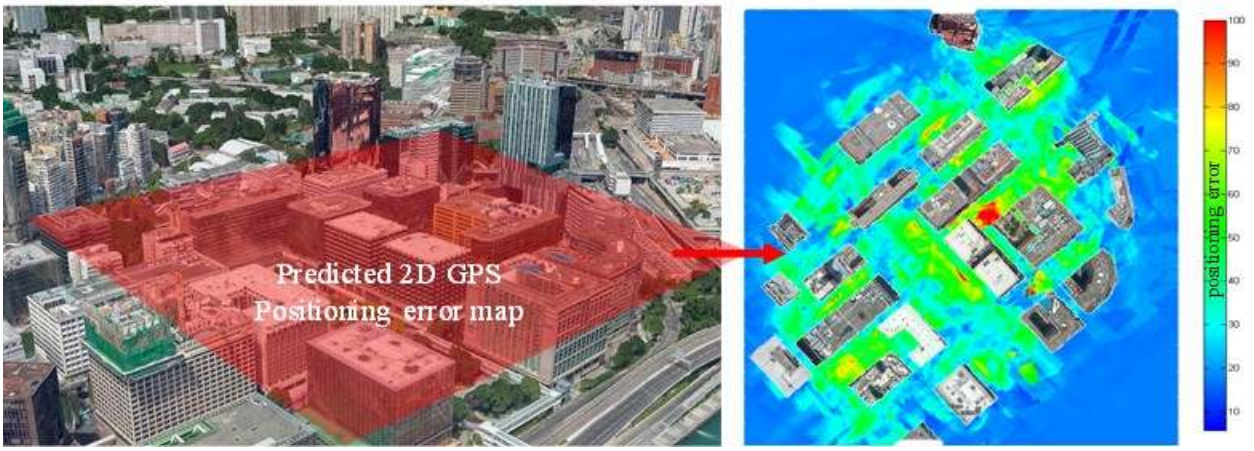

Fig. 4 Demonstration of the prediction of a 2D GPS positioning error map.

3. Offline Path Planning Based on the Predicted Positioning Error Map

To ensure the safety of the public, a path planning method that can identify the obstacles (buildings in our application) in the operation area is a minimum requirement. Furthermore, the path planning algorithm should also consider other factors, such as the shortest path that experiences a minimum GPS positioning error. The main process of the overall path planning is

shown in Fig. 5. The range of permitted height for the UAV is defined from h_0 to h_{max}. After being provided with the starting take-off point, destination and h_0, the previous predicted positioning error map is used to aid 2D path planning. The path planner will estimate an ideal path for each height until reaching the h_{max}, which is often restricted by governmental law. For example, UAV operation in Hong Kong is limited to under approximately 90 meters, as shown in Fig. 1. Afterwards, we can compare the performance of the optimal path on each height. Finally, the overall path of the selected height can be obtained and output as our planned ideal path for the UAV operation. The proposed 2D path planning algorithm is introduced in section 3.1. The height selection algorithm is detailed in section 3.2.

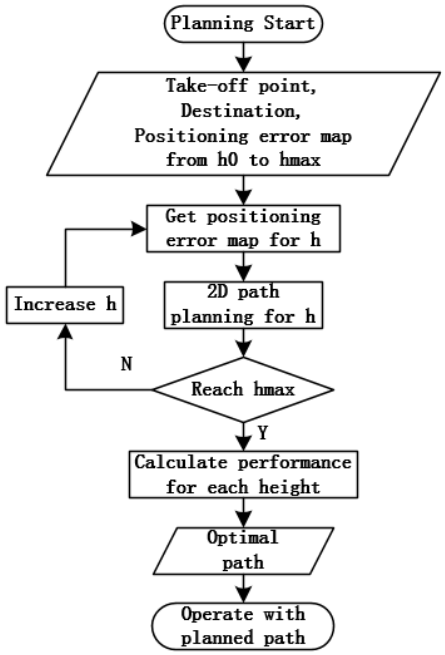

Fig. 5 Flowchart of the proposed 3D path planning for a UAV based on a positioning error map. *h* represents the operating height.

3.1 2D path planning based on A algorithm*

The A* algorithm is a widely used path planning method to avoid obstacles and reach the destination. This method is a global scanning method to obtain a globally optimal path. The overall process of the A* algorithm is shown in Fig. 6.

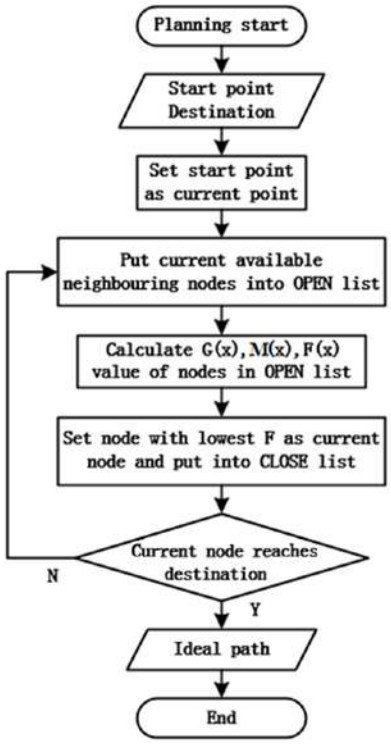

Fig. 6 Flowchart of a conventional 2D A* path planning algorithm.

The conventional A* algorithm constructs a group of nodes (grid points) on the operating map. From the starting node, the A* method identifies whether the neighboring node is available and places all available nodes into an 'open' list. Then, it calculates the cost of all available nodes in the 'open' list. The calculation is shown as:

$$F(n) = G(n) + M(n) \tag{9}$$

$$G(n) = G(n-1) + \|x_n - x_{n-1}\| \tag{10}$$

where n denotes the n^{th} predicted node. $G(n)$ is the minimum traveling distance from the starting node to the current node, and $M(n)$ is the Manhattan distance from the current node to the destination node. The A* algorithm collects all the available nearby nodes into an open list, and the nodes on obstacles will be considered unavailable nodes. By comparing the overall cost value $F(n)$ for the nodes in the 'open' list, the lowest overall cost node will be selected as the next current

node and shifted from the 'open' to the 'close' list. By calculating the cost value again and selecting the next step until the current node reaches the destination, the 'close' list stores all the selected nodes when reaching the destination, and the ideal path can be obtained via extracting nodes from the destination node backwards in the 'close' list.

With the aid of the predicted positioning error map, the positioning error for each node is included in the cost function of the A* algorithm. To ensure the safety of UAVs in an urban area, the major task is to avoid having UAVs crash into buildings. Due to the multipath effect, the UAV can still make contact with buildings by mistakenly recognizing their location. To decrease the potential contacts between UAVs and buildings, the number of contact points *CP* is defined. It is introduced as shown in Fig. 7. For a specific location, its predicted positioning error map is used as a radius of the blue circle, representing the potential GPS positioning error in that specific grid point. When the error circle overlaps with a building, it is considered as one contact point. The number of contact points for a specific location is summed up as *CP*. As shown in Fig. 7, the error circle contacts two neighboring buildings as indicated by the red arrow, namely, *CP* is 2 in this case. The algorithm of the CP calculation is described as follows.

Algorithm 1: Calculation of the number of contact points (CP)	
STEP1:	Input current location x_n and the positioning error ε_n^{pe} at this location
STEP2:	**for** the j^{th} building model in the target area
STEP3:	Initialize contact point number of the j^{th} building at n^{th} location $cp_{n,j} = 0$.
STEP4:	Obtain all the corner locations of the j^{th} building and generate several points between two adjacent corner locations.
STEP5:	**for** the l^{th} generated points of the j^{th} building, $x_{j,l}$
STEP6:	**if** $\left\|x_n - x_{j,l}\right\| \leq \varepsilon_n^{pe}$ **then**
STEP7:	The contact point number of the j^{th} building at n^{th} location $cp_{n,j} = 1$. **break;**
STEP8:	**end if**
STEP9:	**end for** of the l^{th} generated points
	end for of the j^{th} building model
STEP10:	The total contact point number at the n^{th} location for *J* total buildings is $CP(n) = \sum_{j=1}^{J} cp_{n,j}$

The same *CP* calculation can be performed for all locations within the simulated area. Thus, a distribution map of *CP* values can be obtained.

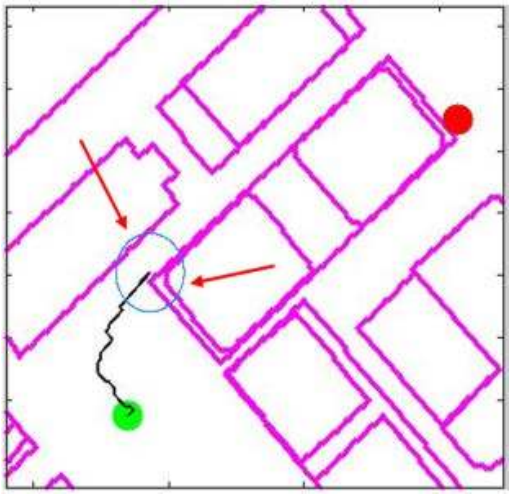

Fig. 7 Contact point (indicated as red arrow) between buildings and error circle (blue circle) on a specific grid point. In this case, *CP* is 2.

The contact number is incorporated into the A* path planning as a part of the cost function. The equation of the traveling cost value *G(n)* is given as:

$$G(n) = [(1 - k_a) \cdot \|x_n - x_{n-1}\| + k_a \cdot \mu_a \cdot CP(n)] + G(n-1) \quad (11)$$

where $\|x_n - x_{n-1}\|$ is the distance between the current node and the next available node and μ_a is a mapping constant to map the effect from the contact point into meters. In this paper, μ_a is heuristically set as 3.7. The weighting k_a can balance the proportion between a shorter traveling distance and a lower contact number, which adapts to different flight requirements. The performance can further adapt to the flight requirements by tuning the weighting value. In this paper, we set k_a as 0.7. $G(n-1)$ is the traveling cost of the parent node with regard to current n^{th} node. To observe (11), the contact numbers can increase the cost value of each approaching

available node. Thus, the path with a large contact number will be avoided by the proposed A* algorithm. $G(n)$ will be further calculated into the overall cost $F(n)$ as (9) to determine the ideal path with the lowest cost. Using the proposed A* path planning algorithm, the ideal 2D path that avoids both the obstacles and the area with a large GPS positioning error can be planned.

3.2 *3D height selection*

To select the ideal height for the UAV operation, the proposed 2D A* path planning will first be applied to each height of the operating area, as shown in Fig. 5. Therefore, the optimal 2D path at each height can be obtained. The performance of the planned path of each height should be evaluated by both the total traveling distance and the total number of potential contact points. We define a cost function *P(h)*, which is a function of height, to determine which height to at which to operate. Its definition is given as:

$$P(h) = (1 - k_a) \cdot \frac{d(h)}{d_0} + k_a \cdot \mu_a \cdot \overline{CP}(h) \tag{12}$$

$$d(h) = \sum_{n_h=1}^{N(h)} \left\| x_{n_h} - x_{n_{h-1}} \right\| + \|h - h_{start}\| + \|h - h_{destination}\| \tag{13}$$

$$d_0 = \|x_{start} - x_{destination}\| \tag{14}$$

$$\overline{CP}(h) = \frac{1}{N(h)} \sum_{n_h=1}^{N(h)} CP(n_h) \tag{15}$$

where $d(h)$ denotes the traveling distance including both the horizontal and vertical movement on the height h by following the planned path and d_0 denotes the direct distance between the starting point and destination. We consider that the lower the cost function is, the better the performance that can be obtained. Good performance means the path can avoid crashing into buildings and reduces the traveling distance at the same time. Hence, we calculate the cost function for the planned path at each height, and then select the height with the lowest cost function as the ideal operating path for the UAV, as shown in (16).

$$h_{ideal} = \arg\min_h P(h) \tag{16}$$

Finally, the optimal path of the selected height and vertical movement for the selected height will be combined as the planned 3D path for UAV operation.

4. Experimental Results and Discussions

4.1 *System architecture of the UAV applying the proposed path planning method*

The system architecture is shown in Fig. 8. The operations are divided into online and offline phases. In the offline phase, GNSS ephemeris data and the 3D building models of the operating periods and areas should be first prepared. By applying the ray-tracing algorithm, the predicted GNSS pseudorange can be simulated for the operating area with different heights during a specific time. The predicted measurements are processed with least square positioning. The predicted positioning solutions of all locations in the operating areas can be simulated. Afterward, the positioning errors for all locations are compared with the true position to generate a positioning error distribution map for different heights. Then, the proposed A* path planning algorithm is applied for the error map of each height to plan a path that optimizes both distance and safety (contact number) on each height. Finally, the optimal 2D + height path that fulfils the requirement is determined by the route with the lowest total cost. After planning the optimal path in the offline phase, the path is sent to the UAV to guide the online navigation.

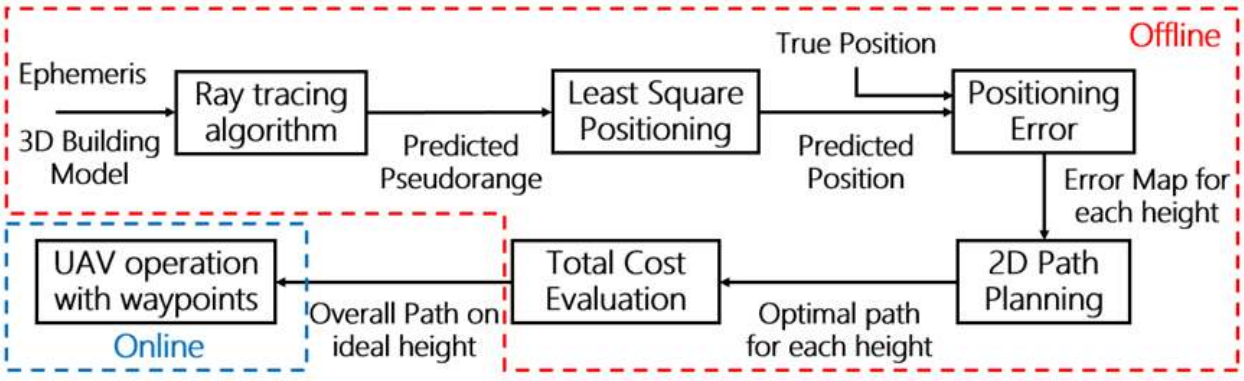

Fig. 8 System architecture of the UAV applying the proposed path planning method.

4.2 *Verification of the prediction of GPS positioning error*

To verify the prediction of the GPS positioning error, experiments are conducted to collect real GPS data in the target area. In this study, we use u-blox NEO-M8T GNSS module as shown in Fig. 9 to receive GPS positioning data. u-blox is a commercial grade receiver that is popular for UAV applications.

Fig. 9 u-blox NEO M8T GNSS module with antenna.

We selected 2 typical locations, intersection and canyon, in an urban canyon to collect data for 30 minutes. The receiver is set at the height of 2 meters to avoid disturbance from pedestrians. The experiment and predicted positioning result are shown in Figs. 10 and 11, respectively. The intersection is in a relatively open area. As shown in Fig. 10, the result of the experiment shows the positioning error is smaller compared to that in the narrow canyon. The left side of Fig. 10 shows that the predicted error is very similar to the actual positioning error. The narrow canyon is surrounded by high buildings, which resulted in a larger positioning error compared to the intersection one. The predicted error in the narrow canyon in also large, agreeing with the experimental result. The comparison between the real (experimental) and predicted GPS positioning error is listed in Table 2. While the device in the experiment could be disturbed by other factors such as foliage, our prediction only considers the multipath effect. Thus, it is reasonable that the experimental error may larger than the prediction error. In general, the overall tendency of the positioning error is similar between prediction and experiment. As a result, the predicted GPS error is verified to model the positioning error distribution.

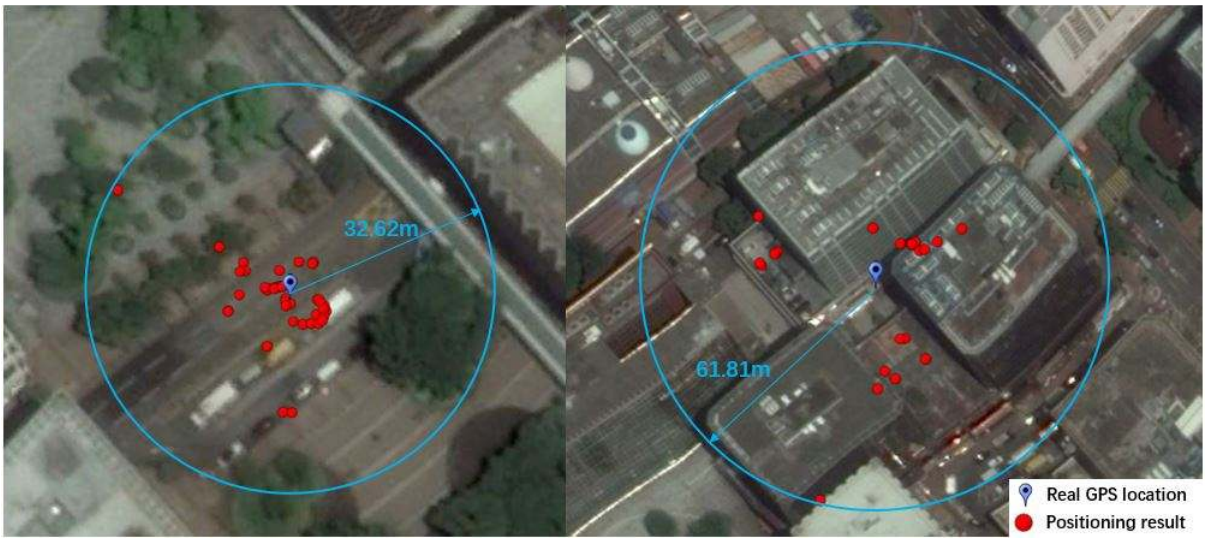

Fig. 10 Experimental GPS positioning result for 30 minutes. The left and right panels show the results in the intersection and the narrow canyon, respectively. Red spots show the positioning result, and the blue balloon shows the real GPS location.

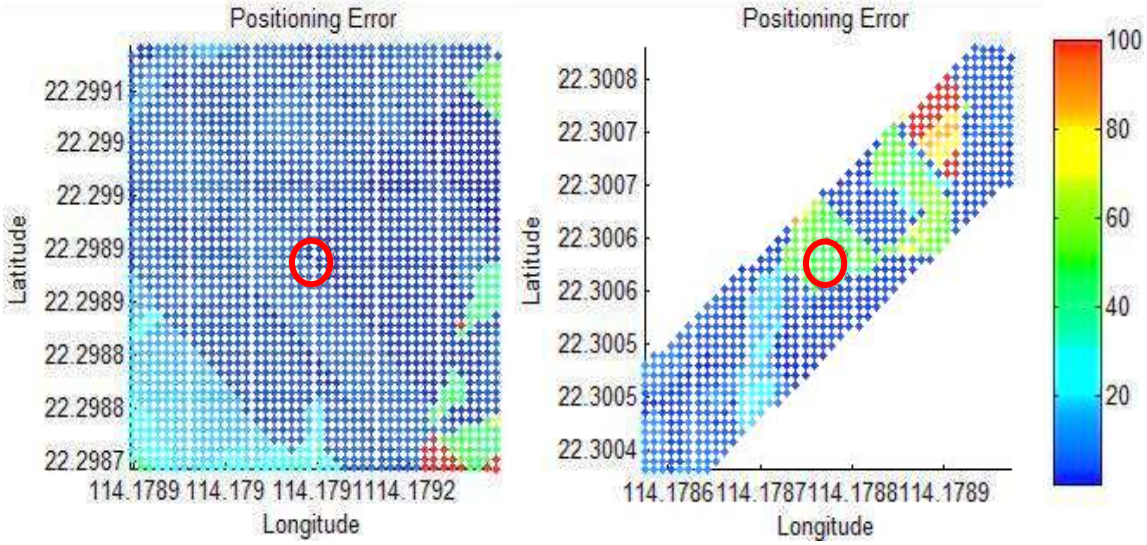

Fig. 11 Predicted positioning error for the experiment location. The left and right panels show the results in the intersection and the narrow canyon, respectively. The color bar denotes the positioning error in meters.

Table 2 Comparison between actual and predicted GPS positioning error.

	Experiment		Prediction
	Mean positioning error (m)	**Max positioning error (m)**	**Mean positioning error (m)**
Intersection (in Fig. 10)	6.38	32.62	5.25
Narrow canyon 1 (in Fig. 10)	24.68	61.81	42.33
Open-sky area	2.64	4.74	0.01
Urban area 1	8.04	28.04	9.67
Urban area 2	14.79	43.53	15.64
Narrow canyon 2	43.05	137.85	42.34
Narrow canyon 3	47.35	76.36	49.06

4.3 *Processing the predicted positioning error map*

Using the proposed UAV path planning algorithm, the 2D positioning error maps at different heights are acquired, as shown in Fig. 12. As the height increases, the overall positioning error is reduced. This is due to the lessened multipath effect and the increasing number of direct signals at higher altitude. When the height is over 50 meters, the predicted error for most of the area is reduced to almost zero since most of the buildings are built within the height of 50 meters in this experimental area. We select two grids to better demonstrate the decrease of GPS positioning error, as shown as Fig. 13. In the case of an open field (blue line), the multipath signal ratio is increased at the height of 25 meters. Then, it continues decreasing as the height increases. The positioning error also follows the same tendency. In the case of the grid nearing the buildings (red line), the positioning error is large on the ground. It starts to decrease after exceeding 22 meters in height. The error slightly increases between 37 and 47 meters in height due to the increase in the multipath ratio and total signal. When the height is increasing, the positioning error can increase in a few situations. This is due to the receiver receiving more NLOS signal at the lower altitude. Thus, the ratio of the multipath signal is increased, resulting in a larger error. Thus, the multipath effect cannot always be considered to decrease as the flying height increases. In the other words, it may not always follow the rule of the higher the better. This paper uses path planning performance to select the ideal height for operation, as described in section 3.3.

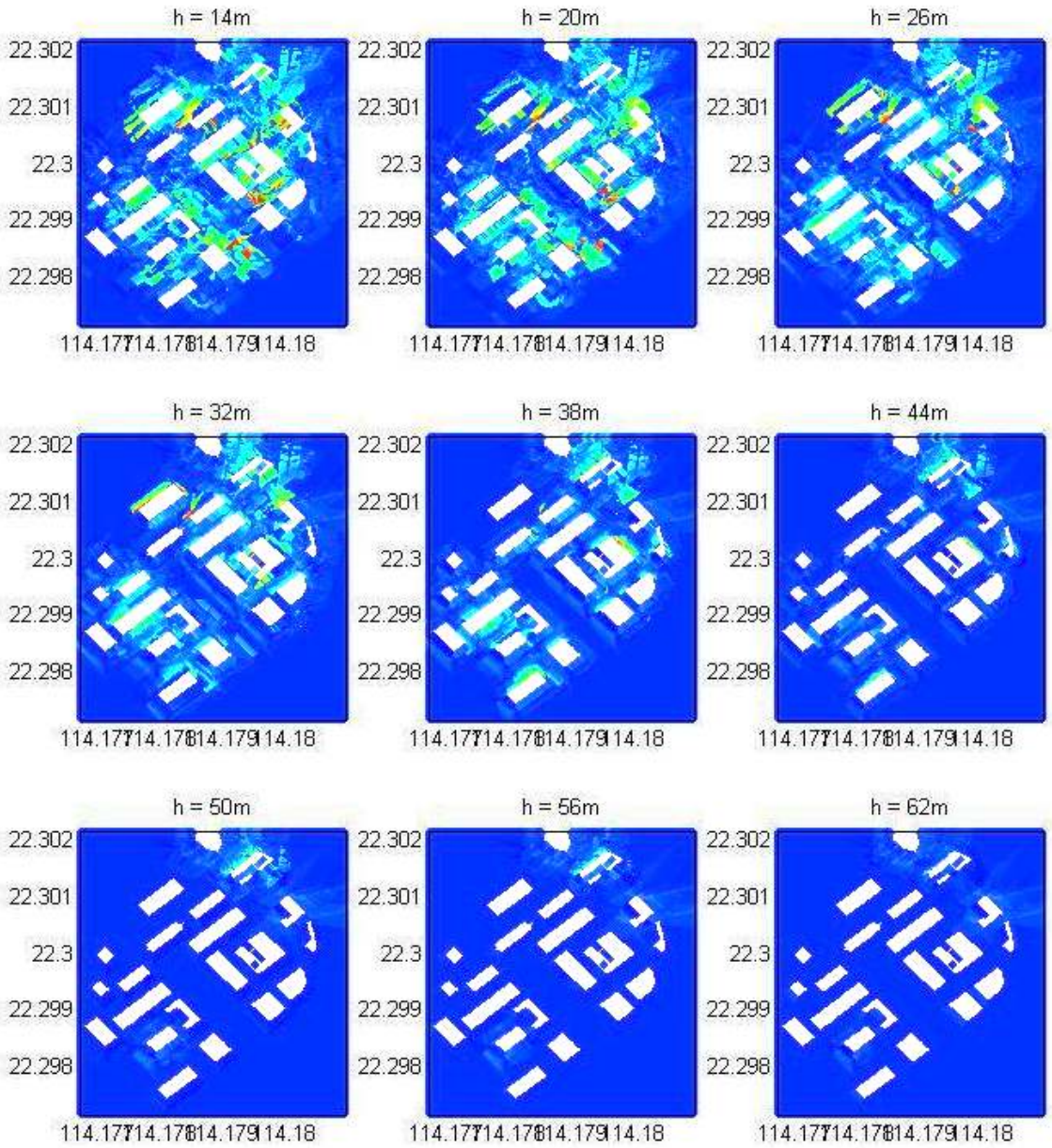

436

437 **Fig. 12** 2D positioning error map at heights between 14 and 62 meters. The resolution is 6 meters
438 for each layer. The color in the figures denotes the predicted positioning error.

439

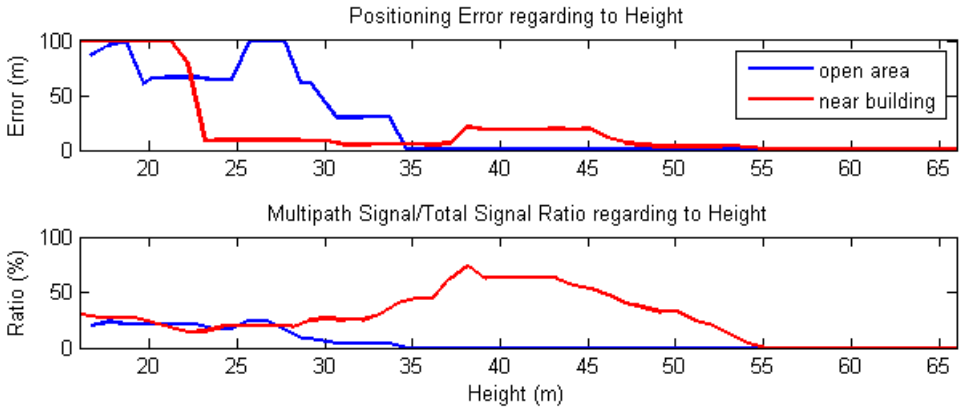

Fig. 13 Demonstration of the relationship between positioning and flight height. Blue and red lines indicate the results of locations at an open area and nearby buildings, respectively.

4.4 *Evaluation of the proposed 2D path planning methods.*

There are three algorithms that were compared:

1. Conventional A* algorithm – using building information as an obstacle
2. Conventional potential field method – using building information
3. Proposed A* algorithm – using both building information and the predicted GPS positioning error map

To apply the proposed path planning algorithm, the positioning error map is predicted for the operation area as shown in Fig. 14. The path planning result of the conventional A* algorithm is shown in Fig. 14. The flight route starts from the star node to the cross node as the dashed line. Without considering the GPS positioning error in path planning, the route is planned directly to the destination, avoiding buildings. The UAV following the planned route may fly through a hazardous zone, such as the red and yellow zones in Fig. 14. The red and yellow zones represent the area where the GPS error exceeded 60 meters. The UAV may mistakenly estimate its location and fly towards the obstacles, causing aircraft to crash when flying through these areas. For the case of the proposed A* algorithm, the path planning result is presented as the solid line in Fig. 14. The UAV can identify the high positioning error area and avoid passing through it. The planned path may experience a longer traveling distance, but it significantly reduces the experienced positioning error in its path. The comparison between the conventional and proposed A* algorithms is shown in Fig. 15. The number of contact points experienced and the positioning error of the proposed A* algorithm are significantly decreased compared with the conventional A*. In

brief, the proposed A* algorithm is able to plan a path with fewer multipath effects, which means traveling on a safer path for UAV operation in an urban area. The performance of each algorithm is listed in Table 3.

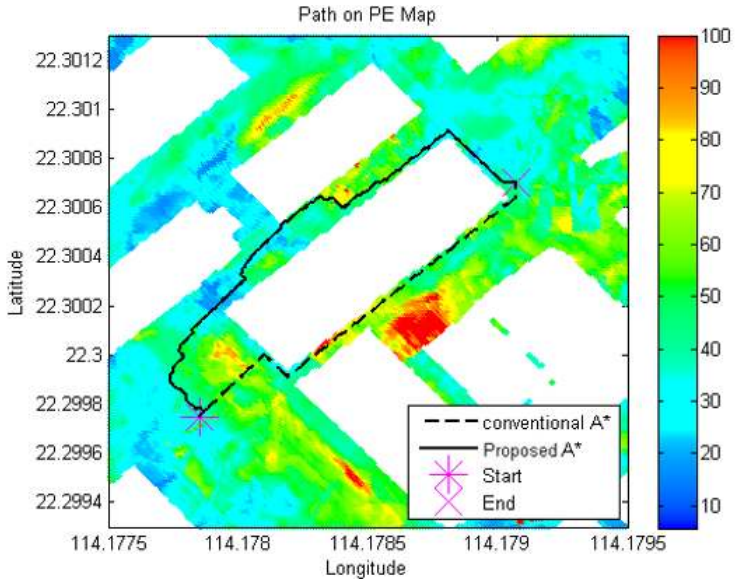

Fig. 14 Conventional and proposed A* path planning algorithm based on a positioning error map. Obstacles (buildings) are constructed as the white area. The color bar denotes the positioning error in meters.

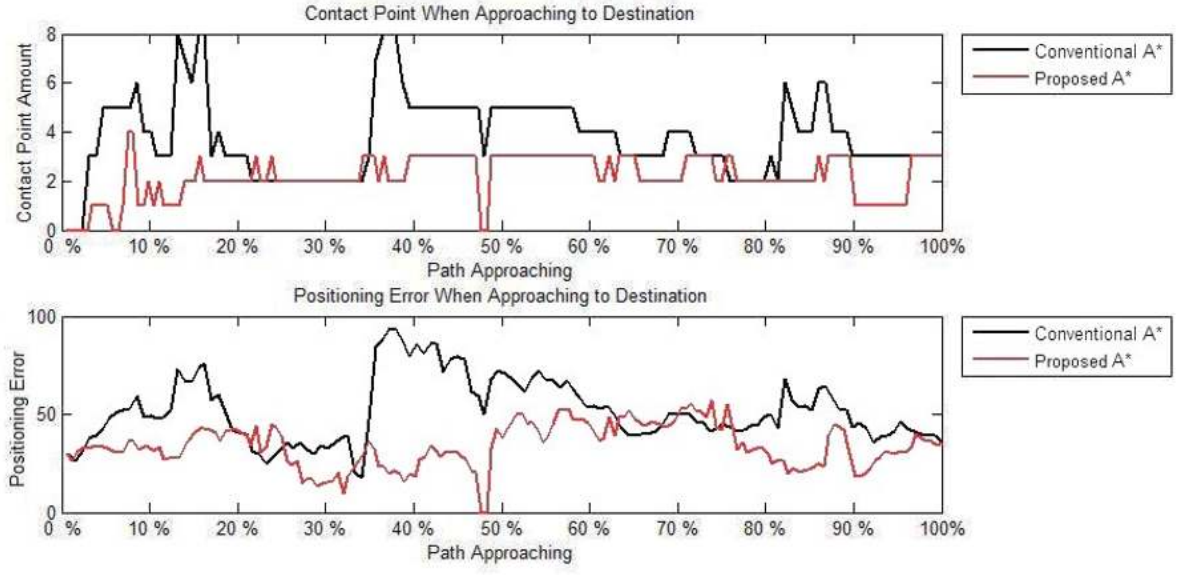

Fig. 15 Contact point number and positioning error comparison between the conventional and the proposed A* algorithms. The x-axis denotes the percentage of the route finished.

476 **Table 3** Performance comparison between different path planning algorithms

	Traveling distance (m)	Mean positioning error (m)	Mean contacting point number
A*	183.64	51.92	3.79
Potential field	164.10	49.91	3.29
Proposed A*	241.41	33.95	2.18

477

478 The potential field method has a better performance than the A* algorithm in terms of traveling
479 distance. From the point of view of safe operation, the proposed A* algorithm designed a route
480 that experienced less GPS positioning error. It results indicate that the potential of contact with
481 buildings (the probability of a crash) is also lower compared to other methods. However, the
482 proposed method requires longer traveling distance to reach the destination. The potential field
483 method has a major limitation, the local optimal problem. This phenomenon usually occurred
484 where the complex geometry of buildings was encountered. Based on the reasons above, we
485 concluded that the proposed A* algorithm is preferential for processing the off-line path planning
486 in an urban area.

487

488 4.5 *Evaluation of 3D path planning result*

489 The 3D path planning means selecting a height layer with the best 2D planning, as introduced in
490 Figs. 1 and 5. The conventional and proposed A* algorithms are evaluated in this subsection. A
491 typical UAV urban transport scenario, with the UAV starting from a ground location and traveling
492 to another ground destination, is tested. The results of the 2D path at different heights are listed in
493 Table 4.

494

495 **Table 4** Performance of the 2D path at different height layers.

Conventional A*										
Height (m)	15	25	35	40	45	50	60	70	**80**	90
Traveling distance(m)	124.6	138.3	158.3	168.3	173.5	183.5	203.5	223.5	**243.5**	263.5
Mean experienced positioning error (m)	17.29	12.54	8.36	5.55	5.05	3.98	3.93	3.79	**3.57**	3.37
Mean contact number	1.073	0.921	0.461	0.427	0.360	0.348	0.348	0.326	**0.281**	0.281
P(h)	3.300	2.927	1.729	1.667	1.498	1.497	1.557	1.555	**1.492**	1.552

Proposed A*										
Height (m)	15	25	35	40	**45**	50	60	70	80	90
Traveling distance (m)	363.37	241.97	197.53	201.43	**210.68**	224.43	241.75	259.69	267.17	282.53
Mean experienced positioning error (m)	6.98	7.70	3.43	4.45	**3.64**	3.08	3.04	2.91	2.41	2.01
Mean contact number	0	0.106	0.062	0.026	**0**	0	0	0	0	0
P(h)	1.082	1.009	0.757	0.671	**0.627**	0.668	0.720	0.773	0.796	0.841

In regard to the observations in Table 4, the experienced positioning error and potential contact number decreased as the height increased. Namely, the risk is smaller when the UAV flies higher. Note that the positioning error during the vertical movement can be neglected because barometer-aided AHRS are usually implemented for the estimation of the UAV's flying altitude. On the other hand, the traveling distance is increased as the height is increased because the vertical traveling distance is also considered. By applying the defined cost function *P(h)*, the compromise between the traveling distance (cost) and the potential contact number (risk) can be determined. The minimum *P(h)* of the conventional A* is 1.492, which occurred in the layer of 80 meters in height. The proposed A* achieves 0.627 of the minimum *P(h)*, which occurred in the layer of 45 meters in height. It is important to note that there is no potential contact point if it flies the path planned by the proposed A* algorithm. Thus, the path planned by the proposed A* not only traveled less distance but also traveled more safely. The planned 2D paths at 80 and 45 meters are shown in the left and right panels of Fig. 16, respectively. In Fig. 16, if the height of a building is higher than the selected height of the planed path, the building will be plotted as a white one. Conversely, when a building is lower than the selected height, it will be plotted as a transparent one. As shown in Fig. 16, there is a high building located on the right side of the planned route. This building reflects GPS signals, resulting in approximately 20 meters of multipath error in its vicinity. The path planned by the proposed method intelligently avoided the area. This capability is important, especially in flying UAVs in an urban area. It can reduce the risks of UAV operation.

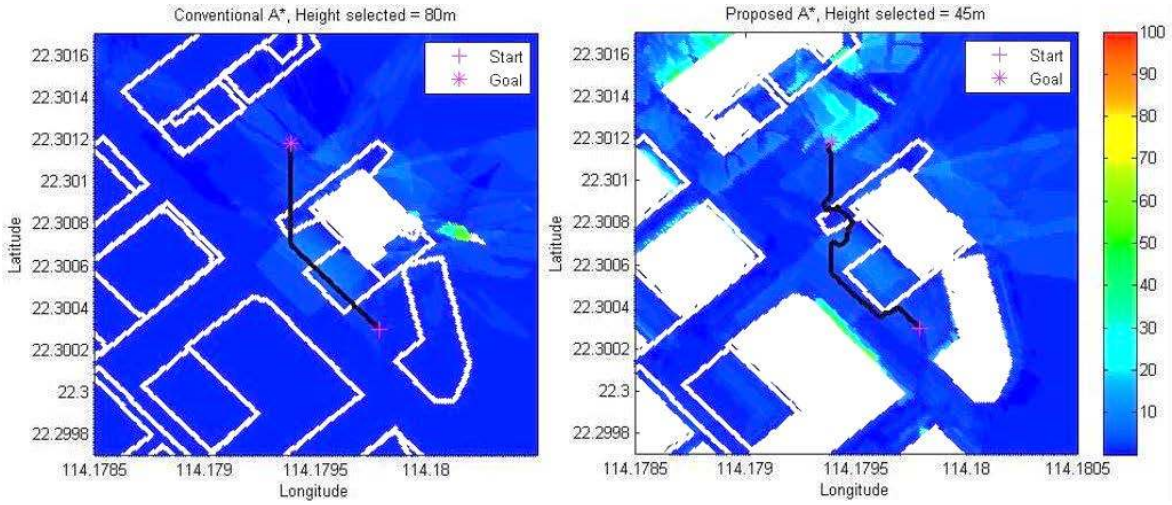

Fig. 16 Results of an operation scenario where the UAV starts from the ground and lands on the ground. Left and right panels demonstrate the conventional A* and the proposed A* methods, respectively.

Different UAV applications have different operating requirements. For example, an urgent medical delivery places more emphasis on distance or asset transportation considers the reliability of operations more than other features. The value of K_a in the cost function indicates the weighting between travel cost and risk. The planning results using different values of K_a are shown in Fig. 17. The corresponding traveling distance, mean contact number and the cost $P(h)$ are shown in Table 5. In the case of K_a=0.7 (the default setting), the planned path is prone to focus on safety. As a result, it selects the height at 60 meters, which has a zero contact number. When reducing K_a to 0.6, the proposed method will determine a height with a balance between the traveling cost and risk. For the case of K_a =0.5, the planned path is prone to focus on shortening the distance.

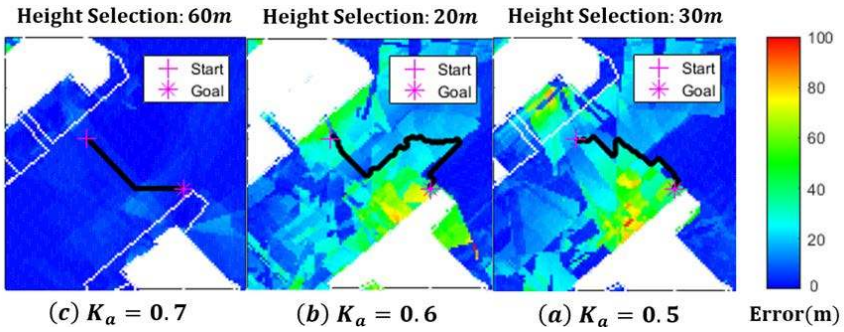

Fig. 17 The planned path results when using different values of K_a. (a), (b) and (c) show the results with K_a equal to 0.5, 0.6 and 0.7, respectively.

Table 5 Performance comparison between different K_a used in the proposed A* path planning method.

h (m)	$d(h)$ (m)	$\overline{CP}(h)$	$P(h)$		
			K_a =0.5	K_a=0.6	K_a =0.7
15	112.45	0.14	1.404	1.224	1.043
20	119.40	0.08	1.363	**1.146**	0.929
25	113.29	0.11	1.373	1.183	0.993
30	100.81	0.15	**1.318**	1.168	1.019
35	106.86	0.18	1.435	1.284	1.133
40	153.46	0.08	1.714	1.427	1.141
45	126.29	0.09	1.463	1.238	1.012
50	127.57	0.08	1.462	1.231	1.001
55	130.77	0.07	1.476	1.235	0.994
60	140.77	0	1.443	1.155	**0.866**
65	150.77	0	1.546	1.237	0.989

4.6 *Verification of the proposed path planning algorithm with a real dataset*

The Hong Kong civil aviation department prohibits UAV operation in urban areas. A feasible approach to verify the proposed method is to conduct an experiment on the ground. In the other words, the quadcopter is carried by a pedestrian to collect the real data and use it to verify the approach. First, the starting position and the destination are selected. GNSS ephemeris is downloaded from the Internet to simulate the GNSS measurements using the 3D building model and the ray-tracing algorithm. The simulated GNSS measurements of different locations are applied with the least square positioning method to generate a positioning error distribution map. Based on the positioning error map, two different paths can be planned by both the conventional and the proposed A* algorithms. Afterward, two pedestrians carry two of the same type of devices and follow the planned paths from the two A* algorithms to collect the GNSS measurement. Finally, the collected data are analyzed to compare with the simulation results in terms of the mean positioning error along the two planned paths. The paths planned by the conventional and the proposed A* algorithms are shown in Fig. 18. The GNSS positioning results of the real dataset collected by following the planned paths are shown in Fig. 19. The comparison between the simulation and real experiment is provided in Table 6.

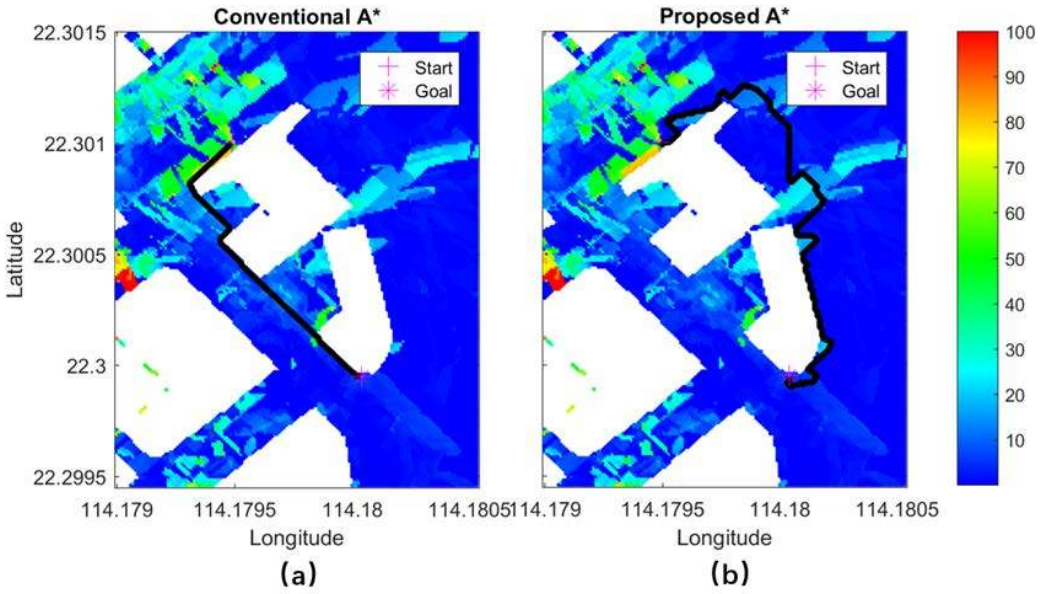

Fig. 18 The paths planned by (a) the conventional A* algorithm and (b) the proposed A* algorithm with the predicted GNSS positioning error map.

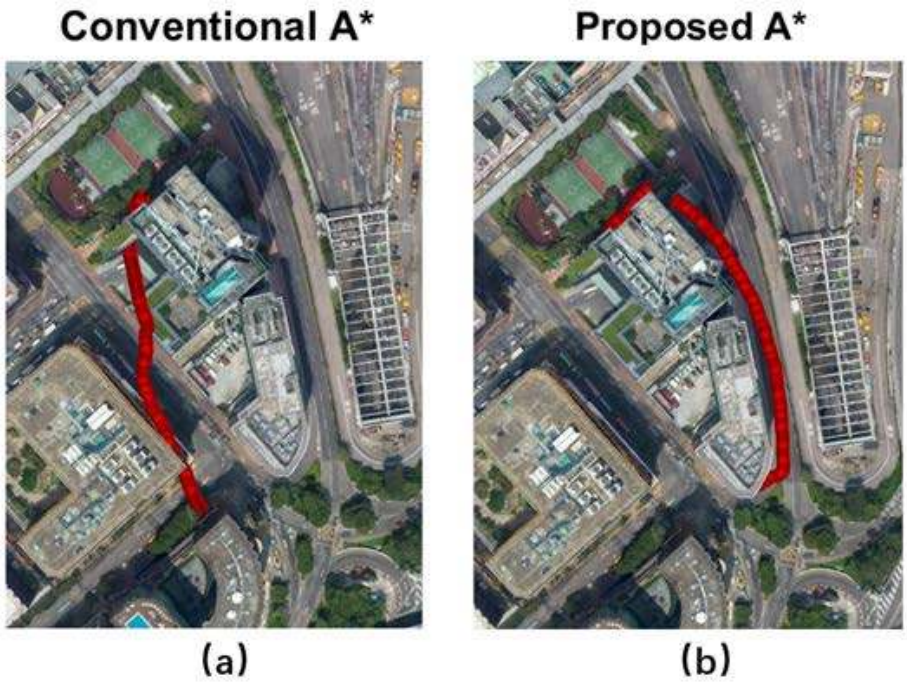

Fig. 19 The real GNSS positioning result provided by the GNSS receiver embedded on the quadcopters. (a) and (b) show the GNSS solutions collected in the paths planned by (a) the conventional and (b) the proposed A* algorithm, respectively.

Table 6 Comparison of the mean predicted positioning error based on the proposed GNSS positioning error map and the mean real collected positioning error calculated by the GNSS receiver.

Simulation		Experiment	
Conventional A*	**Proposed A***	**Conventional A***	**Proposed A***
19.43 meters	**2.62 meters**	**17.52 meters**	**4.94 meters**

As shown in Fig. 18, the proposed A* algorithm can plan a safer path to avoid high GNSS error area compared with the direct path planned by the conventional A* algorithm. The mean experienced positioning errors are 2.62 and 19.43 meters for the proposed and conventional algorithms, respectively. By following the planned paths in the real field test, the GNSS solution with 4.94 meters of mean positioning error is collected in the path planned by the proposed A*, while 17.52 meters of that is collected in the path of the conventional A*. As a result, the predicted and collected positioning errors are very similar, which verifies the feasibility of the proposed A* algorithm in planning safer paths for UAV operation in urban areas.

5. Conclusions

In this study, the multipath effect of GPS positioning in an urban area is modeled and predicted using a 3D building model, ray-tracing simulation and the broadcast almanac. With these tools, the GPS positioning result can be predicted. The prediction is verified by comparing it with the actual GPS positioning error at an intersection and a narrow canyon in the urban area of Kowloon, Hong Kong. In the verification, the actual and predicted positioning errors have a similar level and tendency. This paper proposes a new A* path planning algorithm considering both the maps of the obstacle and the potential GPS positioning error. According to the experimental result, the proposed algorithm is able to determine an ideal path to avoid being positioned in a hazardous area. Thus, it is more preferable for the safety of an operation compared with other path planning algorithms, such as the conventional A* and the potential field methods. In the UAV mission, we suggest that the quadcopter first performs its take-offs vertically to a certain height. Then, it can fly horizontally to the 2D position of the destination. Finally, it lands vertical to the destination. Based on this idea, a new 3D path planning method is developed using the result of the 2D A* algorithm. Typical UAV transporting scenarios are tested. Comparing the results of the

conventional and proposed 3D A* algorithms, the latter approach achieves higher safety at a lower height. In other words, the proposed A* path planning method outperforms the conventional technique.

However, the presented method still has the following drawbacks: 1) The high computational load for the GPS error prediction map required preprocessing before the flight; 2) The planned path may have had a sharp turning angle, which introduced an energy loss for the quadrotor. Additionally, other UAV platforms might not be valid for using the proposed path planning due to the sharp turning issue; and 3) The proposed method is an offline path planning approach. The online path planning method is still required to adjust to changes in the environment. Regarding the drawbacks, future work will endeavor to improve the trajectory smoothness in the path planning algorithm and to integrate sensors for dynamic detection. On the other hand, the lower bound of the positioning error for different GNSS receivers should also be different when applying the prediction of GNSS positioning error in an actual operation. The relationship between the positioning error lower bound and different GNSS receiver types is also worthy of additional investigation. Another interesting concept for future work is to develop a new path planning method to optimize the 3D flight path instead of the 2D + height approach proposed in this paper.

Acknowledgements

The authors acknowledge the fund of “Fundamental Research on Free Exploration Category of Shenzhen Municipal Science and Technology Innovation Committee (Project No. JCYJ20170818103653507)” to support this research.

Localization Strategy using Low-Cost GNSS Module for UAV

References

1. Erdelj, M. and E. Natalizio. *UAV-assisted disaster management: Applications and open issues*. in *2016 International Conference on Computing, Networking and Communications (ICNC)*. 2016.
2. Cistone, J., *Next Century Aerospace Traffic Management: The Sky is No Longer the Limit.* Journal of Aircraft, 2004. **41**(1): p. 36-42.
3. Chiang, K.-W., T. Duong, and J.-K. Liao, *The Performance Analysis of a Real-Time Integrated INS/GPS Vehicle Navigation System with Abnormal GPS Measurement*

Elimination. Sensors, 2013. **13**(8): p. 10599.
4. Kaplan, E. and C. Hegarty, *Understanding GPS: principles and applications*. 2005: Artech house.
5. Hsu, L.T., et al., *Multiple Faulty GNSS Measurement Exclusion Based on Consistency Check in Urban Canyons.* IEEE Sensors Journal, 2017. **17**(6): p. 1909-1917.
6. Christian, E., K. Lasse, and K. Heiner, *Real-Time Single-Frequency GPS/MEMS-IMU Attitude Determination of Lightweight UAVs.* Sensors, 2015. **15**(10): p. 26212-26235.
7. Birk, A., et al., *Safety, Security, and Rescue Missions with an Unmanned Aerial Vehicle (UAV).* Journal of Intelligent & Robotic Systems, 2011. **64**(1): p. 57-76.
8. Song, Y., et al., *Towards autonomous control of quadrotor unmanned aerial vehicles in a GPS-denied urban area via laser ranger finder.* Optik - International Journal for Light and Electron Optics, 2015. **126**(23): p. 3877-3882.
9. Leishman, R., T. McLain, and R. Beard, *Relative Navigation Approach for Vision-Based Aerial GPS-Denied Navigation.* Journal of Intelligent & Robotic Systems, 2014. **74**(1): p. 97-111.
10. Zhu, H., H. Xin, and C. Zheng, *Research On UAV Path Planning*. Applied Mechanics and Materials, 2011. **58-60**: p. 2351.
11. Medeiros, F. and J. Silva, *Computational Modeling for Automatic Path Planning Based on Evaluations of the Effects of Impacts of UAVs on the Ground.* Journal of Intelligent & Robotic Systems, 2011. **61**(1): p. 181-202.
12. Moon, S., E. Oh, and D. Shim, *An Integral Framework of Task Assignment and Path Planning for Multiple Unmanned Aerial Vehicles in Dynamic Environments.* Journal of Intelligent & Robotic Systems, 2013. **70**(1): p. 303-313.
13. Dong, Z., et al. *A hybrid approach of virtual force and A* search algorithm for UAV path re-planning*. in *2011 6th IEEE Conference on Industrial Electronics and Applications*. 2011.
14. Khuswendi, T., H. Hindersah, and W. Adiprawita. *UAV path planning using potential field and modified receding horizon A* 3D algorithm*. in *Proceedings of the 2011 International Conference on Electrical Engineering and Informatics*. 2011.
15. Lin, C.L., et al. *Flight path planning for mini rotor UAVs*. in *11th IEEE International Conference on Control & Automation (ICCA)*. 2014.
16. Meister, O., et al. *Adaptive path planning for a VTOL-UAV*. in *2008 IEEE/ION Position, Location and Navigation Symposium*. 2008.
17. Filippis, L., G. Guglieri, and F. Quagliotti, *Path Planning Strategies for UAVS in 3D Environments.* Journal of Intelligent & Robotic Systems, 2012. **65**(1): p. 247-264.
18. Xia, L., et al. *Path planning for UAV based on improved heuristic A* algorithm*. in *2009 9th International Conference on Electronic Measurement & Instruments*. 2009.
19. Ten Harmsel, A.J., I.J. Olson, and E.M. Atkins, *Emergency Flight Planning for an Energy-Constrained Multicopter.* J Intell Robot Syst, 2016.
20. De Filippis, L., G. Guglieri, and F. Quagliotti, *A Minimum Risk Approach for Path Planning of UAVs.* Journal of Intelligent & Robotic Systems, 2011. **61**(1): p. 203-219.
21. Tseng, F.H., et al. *A Star Search Algorithm for Civil UAV Path Planning with 3G Communication*. in *2014 Tenth International Conference on Intelligent Information Hiding and Multimedia Signal Processing*. 2014.
22. Krawiec, B., K. Kochersberger, and D. Conner, *Autonomous Aerial Radio Repeating Using an A*-Based Path Planning Approach.* Journal of Intelligent & Robotic Systems, 2014. **74**(3): p. 769-789.

23. Hawa, M., *Light-assisted A* path planning.* Engineering Applications of Artificial Intelligence, 2013. **26**(2): p. 888-898.
24. Sun, X., C. Cai, and X. Shen, *A New Cloud Model Based Human-Machine Cooperative Path Planning Method.* Journal of Intelligent & Robotic Systems, 2015. **79**(1): p. 3-19.
25. Zhan, W., et al., *Efficient UAV Path Planning with Multiconstraints in a 3D Large Battlefield Environment.* Mathematical Problems in Engineering, 2014. **2014**.
26. Kunchev, V., et al. *Path planning and obstacle avoidance for autonomous mobile robots: A review*. in *International Conference on Knowledge-Based and Intelligent Information and Engineering Systems*. 2006. Springer.
27. Chen, X. and J. Zhang. *The Three-Dimension Path Planning of UAV Based on Improved Artificial Potential Field in Dynamic Environment*. in *2013 5th International Conference on Intelligent Human-Machine Systems and Cybernetics*. 2013.
28. Montiel, O., R. Sepúlveda, and U. Orozco-Rosas, *Optimal Path Planning Generation for Mobile Robots using Parallel Evolutionary Artificial Potential Field.* Journal of Intelligent & Robotic Systems, 2015. **79**(2): p. 237-257.
29. Mac, T.T., et al. *Improved potential field method for unknown obstacle avoidance using UAV in indoor environment*. in *2016 IEEE 14th International Symposium on Applied Machine Intelligence and Informatics (SAMI)*. 2016.
30. Raja, P. and S. Pugazhenthi, *Optimal path planning of mobile robots: A review.* International Journal of Physical Sciences, 2012. **7**(9): p. 1314-1320.
31. Allaire, F., et al., *FPGA Implementation of Genetic Algorithm for UAV Real-Time Path Planning.* Journal of Intelligent and Robotic Systems, 2009. **54**(1): p. 495-510.
32. Roberge, V., M. Tarbouchi, and G. Labonté, *Comparison of parallel genetic algorithm and particle swarm optimization for real-time UAV path planning.* IEEE Transactions on Industrial Informatics, 2013. **9**(1): p. 132-141.
33. Ismail, A., A. Sheta, and M. Al-Weshah, *A mobile robot path planning using genetic algorithm in static environment.* Journal of Computer Science, 2008. **4**(4): p. 341-344.
34. Tsai, C.-C., H.-C. Huang, and C.-K. Chan, *Parallel elite genetic algorithm and its application to global path planning for autonomous robot navigation.* IEEE Transactions on Industrial Electronics, 2011. **58**(10): p. 4813-4821.
35. Frontera, G., et al., *Approximate 3D Euclidean Shortest Paths for Unmanned Aircraft in Urban Environments.* Journal of Intelligent & Robotic Systems, 2016.
36. Kim, J.-H., S. Sukkarieh, and S. Wishart, *Real-Time Navigation, Guidance, and Control of a UAV Using Low-Cost Sensors*, in *Field and Service Robotics: Recent Advances in Reserch and Applications*, S.i. Yuta, et al., Editors. 2006, Springer Berlin Heidelberg: Berlin, Heidelberg. p. 299-309.
37. Jan, S.s., et al., *Improving GPS-based landing system performance using an empirical barometric altimeter confidence bound.* IEEE Transactions on Aerospace and Electronic Systems, 2008. **44**(1): p. 127-146.
38. Albéri, M., et al., *Accuracy of Flight Altitude Measured with Low-Cost GNSS, Radar and Barometer Sensors: Implications for Airborne Radiometric Surveys.* Sensors, 2017. **17**(8): p. 1889.
39. Zhang, G. and L.-T. Hsu. *A New Path Planning Algorithm Based on GNSS Localization Error Map*. in *ION GNSS+*. 2017. Portland, Oregon.
40. Misra, P. and P. Enge, *Global Positioning System: Signals, Measurements and Performance Second Edition.* Massachusetts: Ganga-Jamuna Press, 2006.

41. Parkinson, B.W. and P.K. Enge, *Differential gps.* Global Positioning System: Theory and applications., 1996. **2**: p. 3-50.
42. Veitsel, V.A., A.V. Zhdanov, and M.I. Zhodzishsky, *The Mitigation of Multipath Errors by Strobe Correlators in GPS/GLONASS Receivers.* GPS Solutions, 1998. **2**(2): p. 38-45.
43. Hsu, L.-T., Y. Gu, and S. Kamijo, *3D building model-based pedestrian positioning method using GPS/GLONASS/QZSS and its reliability calculation.* The Journal of Global Navigation Satellite Systems, 2016. **20**(3): p. 413-428.
44. Hsu, L.-T., *Analysis and modeling GPS NLOS effect in highly urbanized area.* GPS Solutions, 2017. **22**(1): p. 7.
45. Dierendonck, A.J., P. Fenton, and T. Ford, *Theory and Performance of Narrow Correlator Spacing in a GPS Receiver.* Navigation, 1992. **39**(3): p. 265-283.
46. Garin, L., F. van Diggelen, and J.-M. Rousseau. *Strobe and edge correlator multipath mitigation for code*. in *ION GPS-96*. 1996.

Author Biographies

Guohao Zhang received his M.Sc. degree in Mechanical Engineering from Hong Kong Polytechnic University, Hong Kong. He is currently a research assistant with Interdisciplinary Division of Aeronautical and Aviation Engineering, Hong Kong Polytechnic University. His research interests include GNSS localization, UAV navigation, robotics, and multi-sensors integration.

Li-Ta Hsu received the B.S. and Ph.D. degrees in aeronautics and astronautics from National Cheng Kung University, Taiwan, in 2007 and 2013, respectively. He is currently an assistant professor with Interdisciplinary Division of Aeronautical and Aviation Engineering, Hong Kong Polytechnic University, before he served as post-doctoral researcher in Institute of Industrial Science at University of Tokyo, Japan. In 2012 and 2013, he was a visiting scholar in University College London, U.K and Tokyo University of Marine Science and Technology, Japan, respectively. His research interests include GNSS positioning in challenging environments and localization for autonomous driving vehicle and unmanned aerial vehicle.